PAPER

Effect of carbon nano tube working electrode thickness on charge transport kinetics and photo-electrochemical characteristics of dye-sensitized solar cells

To cite this article: Yahia Gacemi *et al* 2018 *Mater. Res. Express* **5** 025513

Materials Research Express

PAPER

RECEIVED
28 November 2017

REVISED
2 February 2018

ACCEPTED FOR PUBLICATION
8 February 2018

PUBLISHED
21 February 2018

Effect of carbon nano tube working electrode thickness on charge transport kinetics and photo-electrochemical characteristics of dye-sensitized solar cells

Yahia Gacemi[1], **Ali Cheknane**[1,3] **and Hikmat S Hilal**[2,3]

[1] Laboratoire des Semiconducteurs et Matériaux Fonctionnels. Université Amar Telidji de Laghouat. Algérie
[2] SSERL, Chemistry Department, An-Najah National University, Nablus, Palestine
[3] Authors to whom any correspondence should be addressed.

E-mail: cheknanea@gmail.com **and** hshilal@najah.edu

Keywords: dye-sensitized solar cell DSSC, carbon nanotube DSSC, PEC, charge transport, mass transfer, film electrode thickness

Abstract

Physiochemical processes at the photo-electrode and the counter electrode of dye sensitized solar cells (DSSCs) involving having carbon nanotubes (CNTs) instead of the TiO_2 layer, within the working electrode, are simulated in this work. Attention is paid to find the effect of CNT layer thickness on photo-electrochemical (PEC) characteristics of the CNT-DSSCs. Comparison with other conventional TiO_2-DSSC systems, taking into account the working electrode film thickness, is also described here. To achieve these goals, a model is presented to explain charge transport and electron recombination which involve electron photo-excitation in dye molecules, injection of electrons from the excited dye to CNT working electrode conduction band, diffusion of electrons inside the CNT electrode, charge transfer between oxidized dye and (I^-) and recombination of electrons. The simulation is based on solving non-linear equations using the Newton-Raphson numerical method. This concept is proposed for modelling numerical Faradaic impedance at the photo-electrode and the platinum counter electrode. It then simulates the cell impedance spectrum describing the locus of the three semicircles in the Nyquist diagram. The transient equivalent circuit model is also presented based on optimizing current–voltage curves of CNT-DSSCs so as to optimize the fill factor (*FF*) and conversion efficiency (η). The results show that the simulated characteristics of CNT-DSSCs, with different active CNT layer thicknesses, are superior to conventional TiO_2-DSSCs.

1. Introduction

Dye-sensitized solar cells (DSSCs) are photo-electrochemical (PEC) cells involving working electrodes based on mesoporous nano-structured semiconductor polycrystalline films deposited onto transparent conducting oxide substrates (TCOs) [1, 2]. Simulation of solar cells helps understand, design and enhance new devices with higher efficiency. Since their emergence [3], DSSCs are potentially useful third-generation solar energy devices.

The performance of a given DSSC demands efficient visible light harvesting, efficient electron-hole separation, fast charge transport and slow electron-hole recombination. This is achievable by choosing the proper materials. In conventional DSSCs the working electrode is a mesoporous semiconductor film, such as those of TiO_2 or ZnO, deposited onto a TCO substrate [4]. Ion transportation occurs by the solution redox couple. Electron diffusion length is determined by electron transport and recombination process competition [5–8].

High quantum efficiency can be achieved, having short-circuited conditions, with electron diffusion length higher than semiconductor film thickness. In case of semiconductor film working electrodes, having high electrolyte concentrations, electron transport should occur mainlythrough diffusion [9, 10]. Diffusion in conventional DSSCs involves slow transport, compared to mono-lithic electrodes. The diffusion coefficients depend on incident light intensity [11, 12].

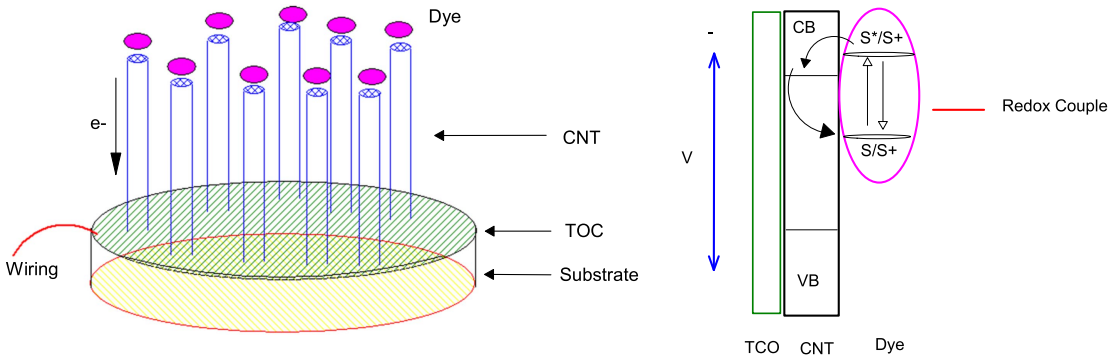

Figure 1. Schematic showing the transport and recombination mechanisms in CNT-DSSCs. The CNT is a replacement for the TiO_2 in the working electrode.

DSSC degradation under PEC working conditions also limits their lifetime and stability. Carbon nanotube based cells (CNT-DSSCs), where the CNT is used as a replacement for the TiO_2 layer, could be an alternative to conventional TiO_2-DSSCs, due to the expected stability and high conversion efficiencies the CNT photo-electrodes (PEs) [13]. CNTs are specially stable with high specific surface area and mechanical durability [14]. They also have tuneable electrical conductivity, and can have metallic or semiconducting properties depending on different factors as their edge types and diameters [15]. CNTs are thus being extensively considered in different contemporary electronic applications [16–19]. With their special electronic properties, CNTs are suitable electrode material candidates [13, 20, 21]. Using CNTs as biosensor electrode materials is reported [22–25]. After the report of Guiseppi-Elie *et al* [21], direct biosensors have gained interest [26]. CNTs have been used as replacement for conventional Pt counter electrodes in TiO_2-DSSCs [27]. Researchers studied the difference between Pt and CNT counter electrodes, from different aspects. However, this topic is not an issue for the present study.

Interfacial charge transfer processes, within DSSCs, were modelled in earlier literature [28]. The models explicitly accounted for each interfacial reaction involving the dye, the redox couple and the electrons in the semiconductor conduction band [28].

The present work describes the Faradaic impedance equation, as derived from the reaction model of PEs and counter electrodes (CEs) in CNT-DSSCs. To describe the frequency response, in terms of electronic and ionic processes in the CNT-DSSC, a theoretical model is given here. To our knowledge such a study has not been reported earlier, and the results here are novel. With the proper equivalent circuits, the charge recombination which limits the efficiency of PEC conversion at the PE can then be simulated and optimized [29, 30]. In an earlier report, CNT-DSSC and TiO_2-DSSC systems have been simulated and compared taking into account the effect of serial resistance [31]. PEC parameters of the CNT-DSSCs will be simulated, and compared here to other reported conventional TiO_2-DSSCs, for the first time to the best of our knowledge, taking into account the thickness of the CNT active layer and the interfacial charge transport and recombination reactions. Effects of other parameters on the solar cell performance deserve additional future study.

2. Interfacial charge transport and recombination reactions at CNT/TCO interface

A DSSC is a PEC system with multi-phase involving (TCO) substrate/dye-sensitized semiconductor film/electrolyte/counter electrode (CE). Figure 1 summarizes a model that describes charge-transfer across the CNT/TCO interface in the working electrode that involves single walled CNTs as replacement for the TiO_2 layer. The interfacial model applies to all interfaces at all points within the PE. The interface involves negligible width within the PE electrode, and has same physical properties at different points.

At the interface, three planes are assumed, all having same electron concentration and potential [28]. The three planes represent the adsorbed redox ions, the CNT surface electrons and the dye molecules. Surface states of the CNT surface corresponding to conduction band are considered, together with oxidized and reduced species within the redox couple.

Figure 1 schematically describes what happens to injected electron from the dye to the CNT. These electrons travel across the CNT film by diffusion and continue their way through the TCO and the metallic wiring [30, 31]. Therefore, in parallel with TiO_2-DSSCs, where excitation occurs for the dye molecules themselves, and the photon-excited electrons travel through the TiO_2 semiconductor layers to reach the metallic wiring, CNT-DSSCs follow similar logic. In their pristine forms, single walled CNT films are known to have transparency

higher than 80% to visible light [32] which allows the photons to reach the dye molecules and cause excitations. Dye molecules may adsorb onto CNT wall surfaces by different methods. Physi-or chemi-sorption may occur at many places on the CNT surface [33]. CNTs are also believed to be 1-dimensional conductors, as conduction is expected to occur along the tube [15]. For these reasons, a dye molecule is assumed to exist onto the opening on the tube, as shown in figure 1. The dye molecules are first excited with visible light, yielding electron-hole pairs. The excited electrons travel along the CNTs to reach the TCO, while the holes travel to oxidize the reduced species in the solution Redox couple. If the electrons do not reach the TCO, and alternatively directly go back to the oxidized dye molecule, or to the oxidized species of the solution Redox couple, electron hole recombination occurs with no charge separation. Such a process lowers the cell efficiency [34]. The main responsibility of the CNT in PEC process is thus to assist transport of the electrons from the excited dye molecules to the TCO and to the external wiring. The transport kinetics is affected by the density of electrons inside the CNT film, which is in turn affected by traps and surface states.

Eelectron diffusion across the CNT film is evaluated by different variables, including recombination assuming appropriate boundary conditions. As stated above, after the working electrode dye is illuminated, electrons are injected into the CNT. The resulting electron density, within the film, is position and time dependent [31]. The continuity equation is then solved using linear geometry, considering a one dimensional system (x-coordinate only). The n_e is the density of conduction band electrons. The differential equation shown below can then be solved [31, 34].

$$D_e \frac{\partial^2 n_e(x,\, t)}{\partial x^2} + G(x) - R(x) = \frac{\partial n_e(x,\, t)}{\partial t} \tag{1}$$

Where $G(x)$ denotes generation rate at a given x distance, $R_e(x)$ is rate of electron recombination as a function of x, D_e is electronic diffusion coefficient ($m^2.s^{-1}$), and $n_e(x, t)$ is electron density (cm^{-3}) as a function of distance (x) from PE surface and time (t) [35].

Generation rate is understood by integrating equation (2), where $\alpha(\lambda)$ is absorption coefficient, n_{inj} is efficiency of electronic injection, $\Phi(\lambda)$ is flux of incident photons, and λ is incident light wavelength [31]:

$$G(x) = n_{inj} \int_{\lambda_{min}}^{\lambda_{max}} \alpha(\lambda)\phi(\lambda)e^{-\alpha(\lambda)x}d\lambda \tag{2}$$

The generation rate is integrated in the wavelength range 3×10^2 to 8×10^2 nm, in which the DSSC may function [36]. Under open circuit conditions the recombination processes readily occur inside the cell solution. The CNT electrons may directly recombine with (I_3^-) ions of the redox couple, or may go to TCO layer and then recombine with the redox species. The recombination process with the I_3^- follows first-order kinetics [36, 37].

$$R(x) = \frac{n_e(x,\, t) - n_{eq}}{\tau_e} \tag{3}$$

Where n_{eq} is the dark electron carrier density at equilibrium, and τ_{e-} is lifetime for electrons determined by reversible reaction with the redox couple I^-/I^-_3.

3. Numerical modeling of faradaic impedance

3.1. Interfacial charge transport reaction at photo-electrode (PE)

The electron injection excited dye electrons into the CNT conduction band is described below [38]:

$$Dye^{\oplus\ominus} + CNT \quad \rightarrow \quad Dye^{+} + CNT^{-}$$
$$The\ injection\ of\ electrons$$

This distinguishes the different steps involved in the mechanism of interfacial reactions in the DSSC. The density of the injected electrons is termed as n_{CNT} ($mol.cm^{-3}$). Such electrons migrate across the CNT thanks to the potential gradient in the space charge layer (SCL). G ($mol.cm^{-2}.s^{-1}$) describes the excitation rate of electrons due to PE irradiation. The dye is thus oxidized simultaneously by electron injection into the CNT. The oxidized dye is then reduced by receiving electrons from I^-. In the PE, reduction of I^-_3 with CNT injected electrons is a charge recombination, a process so-called back electron transfer [38, 39].

Equations of mass balance are derived for the following parameters: electron density within CNT layer surface (n_{CNT} [$mol.cm^{-3}$]), I^- ion concentration at the PE ($C_{I-,PE}$ [$mol.cm^{-3}$]), I^-_3 concentration at the PE surface ($C_{I-3,PE}$ [$mol.cm^{-3}$]), and the oxidized dye ratio (θ).

Two electrochemical reactions are normally considered, at the CNT/Dye interface, and in the mediator. The mass balance equations are useful in describing such behaviors. The first equation helps in determining the variation in the species concentration in a given time [40].

The second equation helps in determining variations in θ and the electron density n_{CNT}, in a given time. The mass balance of $C_{I^-3,PE}$, $C_{I^-,PE}$, θ, and of n_{CNT} is:

$$\begin{cases} h_1 \dfrac{\partial C_{I_3^-,\,PE}}{\partial t} = k_1 C_{I_3^-,\,PE}^3\,\theta^2 - k_2 n_{CNT} C_{I_3^-,\,PE} - J_{I_3^-,\,PE} \\ h_1 \dfrac{\partial C_{I^-,\,PE}}{\partial t} = -3k_1 C_{I_3^-,\,PE}^3\,\theta^2 + 3k_2 n_{CNT} C_{I_3^-,\,PE} - J_{I_3^-,\,PE} \\ n_0 \dfrac{\partial \theta}{\partial t} = (1-\theta)G_0 - 2k_1 C_{I_3^-,\,PE}^3\,\theta^2 \\ h_2 \dfrac{\partial n_{CNT}}{\partial t} = (1-\theta)G_0 - 2k_2 n_{CNT} C_{I_3^-,\,PE} - n_{CNT}\mu_e \sqrt{\dfrac{2qN_D(E_a - E_{fb})}{\varepsilon_s}} \end{cases} \tag{4}$$

Where $J_{I^-3,\,PE}$ [mol.cm^{-2} s^{-1}] is I^-_3 flux, $J_{I^-,PE}$ [mol.cm^{-2} s^{-1}] is the I^- flux, h_1[cm] is layer thickness for electrochemical reactions at the PE surface, h_2[cm] is the CNT film diameter, μ_e [cm^2.V^{-1} s^{-1}] is mobility of the electrons inside the CNT film, and G_0 [mol.cm^{-2} s^{-1}] is electron excitation rate by light with no oxidized dye ($\theta = 0$) [40].

Furthermore, n_0 [mol.cm^{-2}] is concentration of the dye adsorbed at the surface, k_1 [cm^7.mol^{-2} s^{-1}] is the rate constant for I^- oxidation, and k_2[cm^4.mol^{-2} s^{-1}] is rate constant I^-_3 reduction. The k_1 and k_2 potential-independent rate constants. This is because the I^-/I^-_3 redox potential and flat-band potential V_{fb} have constant values [40, 41].

Based on equation (4), the steady-state mass balances of $C_{I^-,PE}$, $C_{I^-3,PE}$, θ and n_{CNT} are described in equation (5). For $C_{I^-,PE}$, $C_{I^-3,PE}$, θ and n_{CNT}, the steady states are written as $\overline{C}_{I_3^-,\,PE}$, $\overline{C}_{I^-,PE}$, $\overline{\theta}$ and $\overline{n}_{CNT}$ [42, 43]. Values of $\overline{C}_{I_3^-,PE}$, $\overline{C}_{I^-,PE}$, $\overline{\theta}$ and $\overline{n}_{CNT}$ are approximated using the Newton–Raphson method [41–43].

$$\begin{cases} h_1 \dfrac{\partial C_{I_3^-,PE}}{\partial t} = f_1(\overline{C}_{I_3^-,PE},\ \overline{C}_{I^-,PE},\ \overline{\theta},\ \overline{n}_{CNT}) = 0 \\ h_1 \dfrac{\partial C_{I^-,PE}}{\partial t} = f_2(\overline{C}_{I_3^-,PE},\ \overline{C}_{I^-,PE},\ \overline{\theta},\ \overline{n}_{CNT}) = 0 \\ n_0 \dfrac{\partial \theta}{\partial t} = f_3(\overline{C}_{I_3^-,PE},\ \overline{C}_{I^-,PE},\ \overline{\theta},\ \overline{n}_{CNT}) = 0 \\ h_2 \dfrac{\partial n_{CNT}}{\partial t} = f_4(\overline{C}_{I_3^-,PE},\ \overline{C}_{I^-,PE},\ \overline{\theta},\ \overline{n}_{CNT}) = 0 \end{cases} \tag{5}$$

Equation (5) can be re-written, using vectors, in a single expression:

$$f_i(x_i) = 0 \tag{6}$$

Equation (7) gives solution for a system of 4 non-linear equations with 4 unknowns.

Vector x_i involves the independent variables, while the vector f_i involves the functions $f_i(x_i)$:

$$x_i = \begin{bmatrix} \overline{C}_{I_3^-,\,PE} \\ \overline{C}_{I^-,\,PE} \\ \overline{\theta} \\ \overline{n}_{CNT} \end{bmatrix},\ f_i(x_i) = \begin{bmatrix} f_1(\overline{C}_{I_3^-,\,PE},\ \overline{C}_{I^-,\,PE},\ \overline{\theta},\ \overline{n}_{CNT}) \\ f_2(\overline{C}_{I_3^-,\,PE},\ \overline{C}_{I^-,\,PE},\ \overline{\theta},\ \overline{n}_{CNT}) \\ f_3(\overline{C}_{I_3^-,\,PE},\ \overline{C}_{I^-,\,PE},\ \overline{\theta},\ \overline{n}_{CNT}) \\ f_4(\overline{C}_{I_3^-,\,PE},\ \overline{C}_{I^-,\,PE},\ \overline{\theta},\ \overline{n}_{CNT}) \end{bmatrix} = \begin{bmatrix} f_1(x_i) \\ \vdots \\ \vdots \\ f_n(x_i) \end{bmatrix} \tag{7}$$

To solve linear equations, the Newton-Raphson method requires building a matrix, so-called the Jacobian (J) of the system. J is defined as:

$$J = \frac{\partial(f_1, f_2, ..,\ f_n)}{\partial(x_1, x_2, ..,\ x_n)} = \begin{bmatrix} \dfrac{\partial(f_1)}{\partial \overline{C}_{I_3^-,\,PE}} & \dfrac{\partial(f_1)}{\partial \overline{C}_{I^-,\,PE}} & \dfrac{\partial(f_1)}{\partial \overline{n}_{CNT}} & \dfrac{\partial(f_1)}{\partial \overline{\theta}} \\ \dfrac{\partial(f_2)}{\partial \overline{C}_{I_3^-,\,PE}} & \dfrac{\partial(f_2)}{\partial \overline{C}_{I^-,\,PE}} & \dfrac{\partial(f_2)}{\partial \overline{n}_{CNT}} & \dfrac{\partial(f_2)}{\partial \overline{\theta}} \\ \dfrac{\partial(f_3)}{\partial \overline{C}_{I_3^-,\,PE}} & \dfrac{\partial(f_3)}{\partial \overline{C}_{I^-,\,PE}} & \dfrac{\partial(f_3)}{\partial \overline{n}_{CNT}} & \dfrac{\partial(f_3)}{\partial \overline{\theta}} \\ \dfrac{\partial(f_4)}{\partial \overline{C}_{I_3^-,\,PE}} & \dfrac{\partial(f_4)}{\partial \overline{C}_{I^-,\,PE}} & \dfrac{\partial(f_4)}{\partial \overline{n}_{CNT}} & \dfrac{\partial(f_4)}{\partial \overline{\theta}} \end{bmatrix} = \left[\frac{\partial f_i}{\partial x_i}\right]_{n\times n} \tag{8}$$

for $i = 1, .., n$, and $n = 4$.

Assuming $x = x_0$ (a vector) is the first trial for the solution, other successive solution approximations can be made from:

$$\begin{bmatrix} \overline{C}_{I_3^-,\,PE} \\ \overline{C}_{I^-,\,PE} \\ \overline{\theta} \\ \overline{n}_{CNT} \end{bmatrix}_{k+1} = \begin{bmatrix} \overline{C}_{I_3^-,\,PE} \\ \overline{C}_{I^-,\,PE} \\ \overline{\theta} \\ \overline{n}_{CNT} \end{bmatrix}_{k} - \begin{bmatrix} \frac{\partial(f_1)}{\partial \overline{C}_{I_3^-,\,PE}} & \frac{\partial(f_1)}{\partial \overline{C}_{I^-,\,PE}} & \frac{\partial(f_1)}{\partial \overline{n}_{CNT}} & \frac{\partial(f_1)}{\partial \overline{\theta}} \\ \frac{\partial(f_2)}{\partial \overline{C}_{I_3^-,\,PE}} & \frac{\partial(f_2)}{\partial \overline{C}_{I^-,\,PE}} & \frac{\partial(f_2)}{\partial \overline{n}_{CNT}} & \frac{\partial(f_2)}{\partial \overline{\theta}} \\ \frac{\partial(f_3)}{\partial \overline{C}_{I_3^-,\,PE}} & \frac{\partial(f_3)}{\partial \overline{C}_{I^-,\,PE}} & \frac{\partial(f_3)}{\partial \overline{n}_{CNT}} & \frac{\partial(f_3)}{\partial \overline{\theta}} \\ \frac{\partial(f_4)}{\partial \overline{C}_{I_3^-,\,PE}} & \frac{\partial(f_4)}{\partial \overline{C}_{I^-,\,PE}} & \frac{\partial(f_4)}{\partial \overline{n}_{CNT}} & \frac{\partial(f_4)}{\partial \overline{\theta}} \end{bmatrix}^{-1}$$

$$\cdot \begin{bmatrix} f_1(\overline{C}_{I_3^-,\,PE},\ \overline{C}_{I^-,\,PE},\ \overline{\theta},\ \overline{n}_{CNT}) \\ f_2(\overline{C}_{I_3^-,\,PE},\ \overline{C}_{I^-,\,PE},\ \overline{\theta},\ \overline{n}_{CNT}) \\ f_3(\overline{C}_{I_3^-,\,PE},\ \overline{C}_{I^-,\,PE},\ \overline{\theta},\ \overline{n}_{CNT}) \\ f_4(\overline{C}_{I_3^-,\,PE},\ \overline{C}_{I^-,\,PE},\ \overline{\theta},\ \overline{n}_{CNT}) \end{bmatrix} \tag{9}$$

The cell current I is affected by rate of electrons which migrate in the SCL as:

$$I = Fn_{CNT}\mu_e\sqrt{\frac{2qN_D(E_a - E_{fb})}{\varepsilon_s}} \tag{10}$$

Equation (11) is derived from equation (10) by Taylor series expansion, without considering terms of orders higher than second order.

$$\Delta I = F\mu_e\left(\sqrt{\frac{2qN_D(E_a - E_{fb})}{\varepsilon_s}}\,\Delta n_{CNT} + \frac{\overline{n}_{CNT}}{2}\sqrt{\frac{2qN_D}{\varepsilon_s(E_a - E_{fb})}}\,\Delta E_a\right) \tag{11}$$

The Faradaic impedance $Z_{F,PE}$ can then be found by dividing equation (11) by PE potential gradient ΔE_{PE} [41, 44].

$$\frac{1}{Z_{F,PE}} = \frac{\Delta I}{\Delta E_a} = F\mu_e\left(\sqrt{\frac{2qN_D(E_a - E_{fb})}{\varepsilon_s}}\,\frac{\Delta n_{CNT}}{\Delta E_a} + \frac{\overline{n}_{CNT}}{2}\sqrt{\frac{2qN_D}{\varepsilon_s(E_a - E_{fb})}}\right) \tag{12}$$

Equation (12) yields $Z_{F,PE}$ as a function of $\Delta n_{CNT}/\Delta E_a$. Based on equation (5), equation (13) is derived using Taylor series expansion.

$$h_1\frac{d\overline{C}_{I_{3,PE}^-}}{dt} = -6k_1\overline{C}^3{}_{I_{,PE}^-}\overline{\theta}\Delta\theta - 9k_1\overline{C}^2{}_{I_{,PE}^-}\theta^2\Delta C_{I_{,PE}^-} + 3k_2\overline{C}_{I_{3,PE}^-}\Delta n_{CNT} + 3k_2\overline{n}_{CNT} \times \Delta C_{I_{3,PE}^-} - \Delta J_{I_{3,PE}^-} \tag{13}$$

From equation (13), equation (14) is derived using Fourier transformation and division by ΔE_a.

$$\left(j\omega h_1 + 9k_1\overline{C}^2{}_{I_{,PE}^-}\theta^2 + \frac{\Delta J_{I_{,PE}^-}}{\Delta C_{I_{,PE}^-}}\right)\frac{\Delta C_{I_{3PE}^-}}{\Delta E_a} = -6k_1\overline{C}^3{}_{I_{,PE}^-}\overline{\theta}\frac{\Delta\theta}{\Delta E_a} + 3k_2\overline{C}_{I_{3,PE}^-}\frac{\Delta n_{CNT}}{\Delta E_a} + 3k_2\overline{n}_{CNT}\frac{\Delta C_{I_{3,PE}^-}}{\Delta E_a} \tag{14}$$

where j is the unit of imaginary number and ω is the angular frequency. Similarly, equations (15) and (16) can also be derived from equation (4) [37].

$$\left(j\omega h_1 + k_2\overline{n}_{CNT} + \frac{\Delta J_{I_{3,PE}^-}}{\Delta C_{I_{3,PE}^-}}\right)\frac{\Delta C_{I_{3,PE}^-}}{\Delta E_a} = -2k_1\overline{C}^3{}_{I_{,PE}^-}\overline{\theta}\frac{\Delta\theta}{\Delta E_a} - k_2\overline{C}_{I_{3,PE}^-}\frac{\Delta n_{CNT}}{\Delta E_a} + 3k_2\overline{C}^2{}_{I_{,PE}^-}\overline{\theta}^2\frac{\Delta C_{I_{,PE}^-}}{\Delta E_a} \tag{15}$$

$$\left(j\omega n_0 + 4k_1\overline{C}^3{}_{I_{3,PE}^-}\overline{\theta} + G_0\right)\frac{\Delta\theta}{\Delta E_a} = -6k_1\overline{C}^2{}_{I_{,PE}^-}\overline{\theta}^2\frac{\Delta C_{I_{,PE}^-}}{\Delta E_a}\left(j\omega h_2 + 2k_2\overline{C}_{I_{3,PE}^-} + \mu\sqrt{\frac{2qN_D(E_a - E_{fb})}{\varepsilon_s}}\right)\frac{\Delta n_{CNT}}{\Delta E_a} = -G_0\frac{\Delta\theta}{\Delta E_a} - 2k_2\overline{n}_{CNT}\frac{\Delta C_{I_{,PE}^-}}{\Delta E_a} - \frac{\mu\overline{n}_{CNT}}{2} \times \sqrt{\frac{2qN_D}{\varepsilon_s(E_a - E_{fb})}} \tag{16}$$

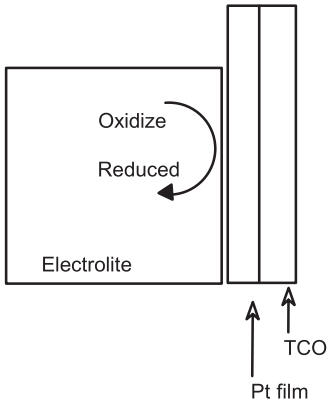

Figure 2. Schematic reaction mass transfer at the Pt/redox couple interface.

And $(\Delta J_{I^-_{,PE}}/\Delta C_{I^-_{,PE}})$ and $(\Delta J_{I^-_{3,PE}}/\Delta C_{I^-_{3,PE}})$ can be found by:

$$\frac{\Delta C_{I^-_{,PE}}}{\Delta J_{I^-_{,PE}}} = (j\omega D_{I^-})^{1/2} \tanh\left\{\gamma_a\left(\frac{j\omega}{D_{I^-}}\right)^{1/2}\right\} \tag{17}$$

$$\frac{\Delta C_{I^-_{3,PE}}}{\Delta J_{I^-_{3,PE}}} = (j\omega D_{I^-_3})^{1/2} \tanh\left\{\gamma_a\left(\frac{j\omega}{D_{I^-_3}}\right)^{1/2}\right\} \tag{18}$$

3.2. Interfacial mass transfer reaction at counter electrode

As electrons diffuse through the redox couple, I_3^- is reduced to I^- at CE. In a DSSC the CE is usually a thin platinum catalytic layer deposited onto a TCO substrate. Over potential is needed to force reduction reaction at a given current density. The kinetic over-potential can be minimized by using a high exchange current density for the redox couple. This manifests the importance of using platinum electrodes, as they behave as charge transfer catalysts. The electron transfer rate from platinum to I_3^- is faster than from the TCO conduction band. Voltage losses may thus occur by diffusion [45, 46].

Recombination of semiconductor excited electrons with I_3^- is the major loss process in a DSSC. In TiO_2-DSSC theoretical and experimental studies of recombination kinetics are focused on I^-/I_3^- redox couple [47]. In case of CNT systems, a two-electron recombination reaction with I^-/I_3^- is assumed as shown equation (A) below:

$$I_3^- + 2e^- \rightarrow 3I^- \tag{A}$$

Two possible intermediate steps may occur for the reaction as shown below. Equation (B) involves an elementary reduction reaction for I^-_3 to iodine radical ion I^-_2.

$$I_3^- + e^- \rightarrow I_2^- + I^- \tag{B}$$

$$I_2^- + e^- \rightarrow 2I^- \tag{C}$$

$$2I_2^- \rightarrow I_3^- + I^- \tag{D}$$

$$3I_3^- \rightarrow I_3^- + 2e^- \tag{E}$$

A multi-step mechanism involving the species I^-_2 is thus expected for electron transfer to I_3^-, with one step being rate determining. Unfortunately, the exact nature of the electron transfer process is not known. Device parameters, such as the dye molecule and the electrolyte solvent, affect the reaction which is believed to be approximately first order with respect to either I^-_2 and I^-_3 [48–50].

The reduction processes that occur at the Pt CE are summarized in figure 2. The redox reaction of I^-/I_3^- may occur via different mechanisms [48–50], and the reactions (A) through (E) are used to calculate the Faradaic impedance here.

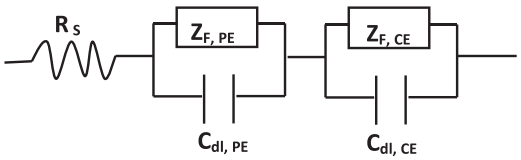

Figure 3. A proposed equivalent circuit of DSSC with Faradaic impedance.

Mass balances of I^- ($C_{I-,CE}$) and I^-_3 ($C_{I-3-,CE}$) concentrations on the CE are [41].

$$\begin{cases} h_3 \dfrac{\partial C_{I^-,CE}}{\partial t} = 3k_3 C^3{}_{I^-,CE} - J_{I^-,CE} \\ h_3 \dfrac{\partial C_{I_3^-,CE}}{\partial t} = -3k_3 C_{I_3^-,CE} + k_{-3} C^3{}_{I_3^-,CE} - J_{I_3^-,CE} \end{cases} \tag{19}$$

At the CE, h_3 describes the reaction layer thickness, while k_3 [cm.s^{-1}] and k_{-3} [cm^7.mol^{-2}.s^{-1}] are potential-dependent rate constants. The rate constants (k_3 and k_{-3}) for the reversible reaction depend on the reactant concentrations and on the rate constants for process.

At steady state $(\partial C_{I^-,CE}/\partial t) = 0$ and $(\partial C_{I_3^-,CE}/\partial t) = 0$, the steady-state mass balances are thus given by:

$$\begin{cases} h_3 \dfrac{\partial C_{I^-,CE}}{\partial t} = g_1(\overline{C}_{I^-,CE}, \overline{C}_{I_3^-,CE}) = 0 \\ h_3 \dfrac{\partial C_{I_3^-,CE}}{\partial t} = g_2(\overline{C}_{I^-,CE}, \overline{C}_{I_3^-,CE}) = 0 \end{cases} \tag{20}$$

Where $x_i = \begin{bmatrix} \overline{C}_{I^-,CE} \\ \overline{C}_{I_3^-,CE} \end{bmatrix}$ is a vector that contains the independent variables.

To solve the linear equations, the Newton-Raphson method requires construction of a matrix defined as:

$$\begin{bmatrix} \overline{C}_{I^-,CE} \\ \overline{C}_{I_3^-,CE} \end{bmatrix}_{k+1} = \begin{bmatrix} \overline{C}_{I^-,CE} \\ \overline{C}_{I_3^-,CE} \end{bmatrix}_{k} - \begin{bmatrix} \dfrac{\partial g_1}{\partial \overline{C}_{I^-,CE}} & \dfrac{\partial g_1}{\partial \overline{C}_{I_3^-,CE}} \\ \dfrac{\partial g_2}{\partial \overline{C}_{I^-,CE}} & \dfrac{\partial g_2}{\partial \overline{C}_{I_3^-,CE}} \end{bmatrix}^{-1} \cdot \begin{bmatrix} g_1(\overline{C}_{I^-,CE}, \overline{C}_{I_3^-,CE}) \\ g_2(\overline{C}_{I^-,CE}, \overline{C}_{I_3^-,CE}) \end{bmatrix} \tag{21}$$

In the CE, the Jacobian matrix (J) for the interfacial reaction system is defined by:

$$J = \frac{\partial(g_1,\ g_2)}{\partial(x_1,\ x_2)} = \begin{bmatrix} \dfrac{\partial g_1}{\partial \overline{C}_{I^-,CE}} & \dfrac{\partial g_1}{\partial \overline{C}_{I_3^-,CE}} \\ \dfrac{\partial g_2}{\partial \overline{C}_{I^-,CE}} & \dfrac{\partial g_2}{\partial \overline{C}_{I_3^-,CE}} \end{bmatrix} = \begin{bmatrix} \dfrac{\partial g_i}{\partial x_i} \end{bmatrix}_{n \times n} \tag{22}$$

for $i = 1, .., n$ and $n = 2$.

For the CE, the charge balance is:

$$I = 2F(k_3 C_{I_3^-,CE} - k_{-3} C^3{}_{I^-,CE}) \tag{23}$$

From equation (23), the following equation can be derived by the Taylor series expansion:

$$\Delta I = -2F(k_3 \Delta C_{I_3^-,CE} + b_3 k_3 \overline{C}_{I_3^-,CE} \Delta E_c - 3k_{-3} \overline{C}^2{}_{I^-,CE} \Delta \overline{C}_{I^-,CE} - b_{-3} k_{-3} \overline{C}^3{}_{I_3^-,CE} \Delta E_c) \tag{24}$$

From the reciprocal of $\Delta I/\Delta E_a$ the Faradaic impedance $Z_{F,CE}$ can be obtained from equation (25).

$$\frac{1}{Z_{F,CE}} = \frac{\Delta I}{\Delta E_c} = -2F\left(k_3 \frac{\Delta C_{I_3^-,CE}}{\Delta E_c} + b_3 k_3 \overline{C}_{I_3^-,CE} - 3k_{-3} \overline{C}^2{}_{I^-,CE} \frac{\Delta \overline{C}_{I^-,CE}}{\Delta E_c} - b_{-3} k_{-3} \overline{C}^3{}_{I_3^-,CE}\right) \tag{25}$$

Figure 3 involves five parameters: total resistance for substrate and solution (R_s), Faradaic impedance for the PE ($Z_{F,PE}$) and for the CE ($Z_{F,CE}$), and values of electric double layer capacitance for PE ($C_{dl,PE}$) and CE ($C_{dl,CE}$).

The impedance values for both the PE (Z_{PE}) and the CE (Z_{CE}) can be found as [37]:

$$Z_{PE} = \frac{Z_{F,PE}(\omega)}{j\omega\ .\ Z_{F,PE}(\omega) C_{dl,PE} + 1} \tag{26}$$

$$Z_{CE} = \frac{Z_{F,CE}(\omega)}{j\omega.Z_{F,CE}(\omega)C_{dl,CE} + 1} \quad (27)$$

Value of cell impedance (Z_{DSSC}) may be obtained based on the equivalent circuit described in figure 3 by:

$$Z_{DSSC} = Z_{PE} + Z_{CE} + R_S \quad (28)$$

Z_{DSSC} involves a real part (Z') and an imaginary part (Z'') related by $Z_{DSSC} = Z' - jZ''$.

4. Results and discussion

Results of numerical modelling impedance spectra the interfacial charge transport and mass transfer model at PE and Pt CE are shown here. Equations of Faradaic impedance for the PE and the CE [19, 22] are derived. DSSC cell impedance and J-V curve simulations are also described to test the assumed equivalent circuit using Faradaic impedance (figure 3). Electrochemical impedance helps to find the effect of different resistances on CNT-DSSC performance.

Two differential equation sets (mass transfer balance equation and migration) can help find Faradaic impedance for electrodes, as described in sections 3.1 and 3.2. An algorithm is shown to observe the electrochemical impedance spectra, as shown below:

Algorithm

Begin

1. Initialization of the physical parameters

.The initial values

x0 = [$\overline{C}_{I_3^-,PE}$, $\overline{C}_{I^-,PE}$, $\overline{\theta}$, $\overline{n}_{CNT}$]; % PE;

x0 = [$\overline{C}_{I_3^-,CE}$, $\overline{C}_{I^-,CE}$]; % CE;

2. **While** ($\omega < \omega_{max}$) **do**

- Array containing the vector independent variables
- given the jacobian function J, with
- x0 is an initial guess of the solution
- epsilon = 1e − 10;
- maxval = 10 000.0;
- xx ← x0;

3. **While** (N < 0) do

JJ = J(xx);

If abs(det(JJ)) < epsilon **then**

error (' newtonm—Jacobian is singular—try new x0 ');

end;

xn ← xx − $(JJ)^{-1}$ × f(xx);

If abs(f(xn)) < epsilon **then**

x ← xn;

iter = 100-N;

return;

end;

If abs(f(xx)) > maxval **then**

iter = 100-N;

error ('Solution diverges');

end;

N ← N + 1;

xx ← xn;

end;

error('No convergence after 1e2 iterations.');

abort;

4. Calculation of Faradaic impedance of the PE (Za)

$Z_{PE} = \frac{Z_{F,PE}(\omega)}{j\omega.Z_{F,PE}(\omega)C_{dl,PE}+1}$

5. Calculation Faradaic impedance of the CE (Zc)

$Z_{CE} = \frac{Z_{F,CE}(\omega)}{j\omega.Z_{F,CE}(\omega)C_{dl,CE}+1}$

6. Calculation Faradaic impedance of the DSSC based on CNT

$Z_{DSC} = Z_{PE} + Z_{CE} + R_S$

$\omega = \omega + 1$;

End.

Table 1. Simulation input parameters.

Input parameter	Value	Reference
k_s	4.43×10^{-12} Fcm^{-1}	[40]
D_{I^-}	4.91×10^{-6} cm^{-1} s^{-1}	[35]
D_{I^-3}	4.91×10^{-6} cm^{-1} s^{-1}	[35]
T	298 K	
$C_{I^-,PE}$	3×10^{-4} mol.cm-3	[41]
$C_{I^-3,PE}$	3×10^{-5} mol.cm-3	[41]
μ_e (*CNT*)	10^8 cm^2 V^{-1} s^{-1}	[13]
De−	$\frac{kT}{e}\mu_e$(cm^{-1} s^{-1})	[13]
G_0	2×10^{-7} mo.lcm^{-2} s^{-1}	[41]
k_1	10^9 mol^{-2} cm^7 s^{-1}	[41]
k_2	10^5 mol^{-2} cm^4 s^{-1}	[41]
N_D	10^{16} cm^{-3}	[51]
δ_a	0.002 cm	[40]
n_0	10^{-8} mol.cm^{-2}	
$C_{I^-,CE}$	3×10^{-4} mol.cm^{-3}	[40]
$C_{I^-3,CE}$	3×10^{-5} mol.cm^{-3}	[40]
N_0	10^{-20} mol.cm^{-3}	[40]
$C_{dl,PE}$	5×10^{-3} F.cm^{-2}	[40]
$C_{dl,CE}$	10^{-4} F.cm^{-2}	[40]
h_2	0.001 μm	

Section 3 described details of the test cell. Unless otherwise stated, the parameter values (all of which are defined above) used in the simulations are those listed in table 1. Faradaic impedance is frequency dependent that is related to the electrode processes, such as photo-excitation, electron transfer, charge transfer and diffusion.

Electrical circuits, with resistors and capacitors, can describe physical and chemical reactions. Interfacial reaction analysis involves response of the system as a function of the frequency. The PE and CE Nyquist diagrams can thus be constructed.

Impedance simulation can be used to study interfacial charge transport and mass transfer reactions in DSSCs. Therefore, the simulation technique has been used for CNT-DSSCs, to study the internal resistances and the interface electron transfer kinetics.

Impedance spectra are simulated here within the frequency range 10^{-2}–10^6 Hz. Based on table (1) parameters, the Faradaic impedance is calculated to model the CNT electrodes, as shown in figure 4.

The equivalent circuit shown in figure 3 is proposed to analyse the DSSC impedance spectrum based on the theoretical understanding of the mechanism of interfacial charge transport and mass transfer. Figure 4 shows the simulation result of the impedance spectrum Z_{PE} (Nyquist diagram), based on table (1) parameters. The Faradaic impedance for the PE ($Z_{F,PE}$), is obtained from simulation using equations (4) and (12), with the Newton- Raphson (MNR). The impedance spectrum shows two loops, one large capacitive loop for high-frequency, and one relatively inductive loop based on lower frequency.

Two competing phenomena occur, namely: electron recombination and electron transport, corresponding respectively to the pulsations ω_{rec} and ω_d. In order to find relative importance of these terms, the value of their ratio can be determined as:

$$\frac{\omega_{rec}}{\omega_d} = \frac{\tau_n}{\tau_d} \tag{29}$$

Where $\tau_n \gg \tau_d$.

Electron lifetime is longer than its transfer time. Therefore, the electrons may transfer before recombination. This is a necessity for a given solar cell to function. This means low transfer resistance R_t and high recombination resistance R_r values. Figure 5 summarizes the simulated Nyquist plot for the Pt CE.

Figures 6 and 7 show the Nyquist plots CNT-DSSC and TiO_2-DSSC cells, respectively, in the low and high frequency ranges. In each case, two main semicircles are observed for Z_{DSSC} impedance spectra in each frequency range. The results can be interpreted as follows: the first semicircle at high frequency range (10^3–10^5 Hz) corresponds to the oxidation/reduction reaction at the electrode, while the second semicircle at low frequency range (1–10^2 Hz) corresponds to charge transfer at the CNT/Dye/electrolyte interface.

Under steady-state conditions of photo-current and photo-voltage, the electron transport (in the CNT film), the electron recombination (with electrolyte at the CNT/electrolyte interface) and electron injection (from excited dye molecules) can be described by equation (1).

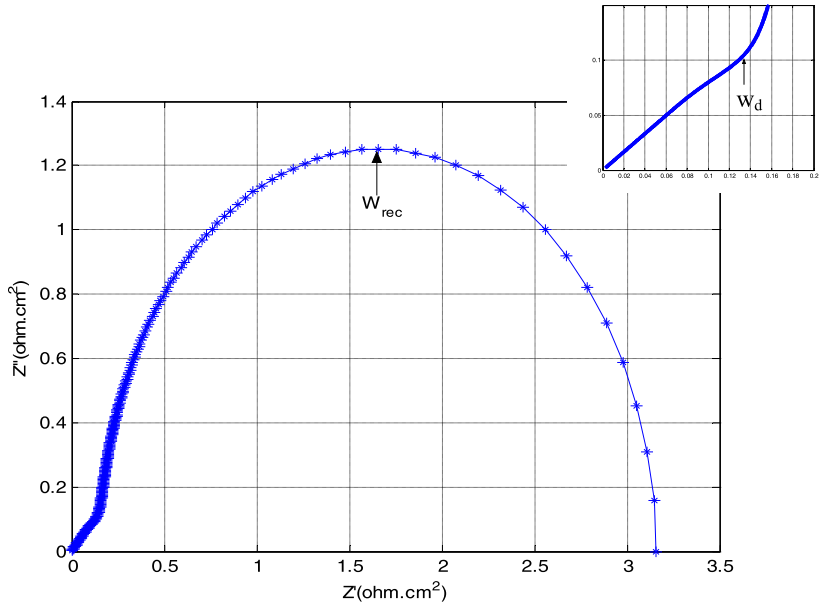

Figure 4. Nyquist diagram for the PEs in CNT.

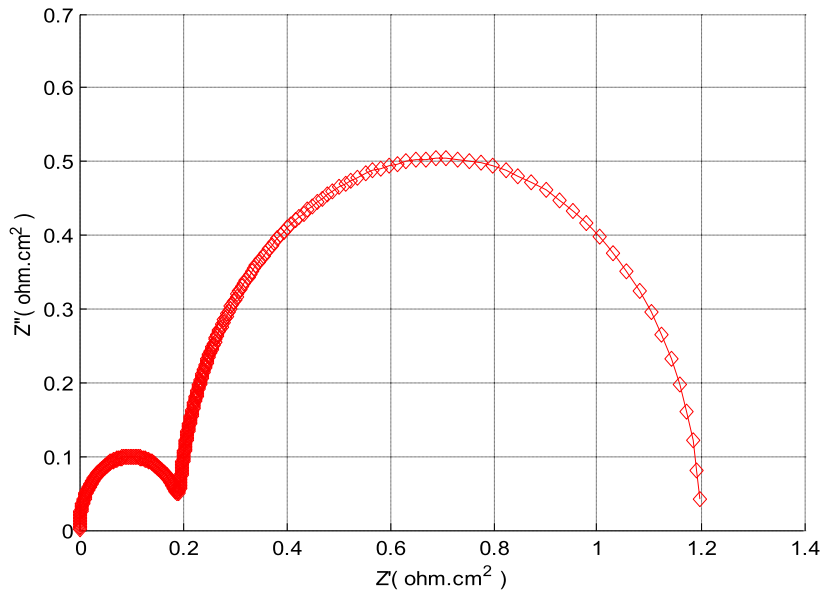

Figure 5. Simulated Nyquist plot for the Pt CE.

The x describes position within the cell, where $x = 0$ shows TCO-CNT interface. The $x = d$ is the thickness of the simulated cell and describes the Pt-TCO/electrolyte interface.

In case of short-circuit, the electron density at the working electrode surface ($x = 0$) at zero time, equals the electron density in case of zero photo-voltage, $n_0 = n(x = 0, V = 0, t = 0) = n(x = 0, V = 0, t)$ [9, 31]. Under conditions of short-circuit, the excited electrons yield photo-current and do not combine with the redox couple.

Boundary conditions are thus:

$$n(0) = \int_{E_c}^{\infty} f_L(E) N(E) dE \tag{30}$$

And

$$\left.\frac{dn}{dx}\right|_{x=d} = 0 \tag{31}$$

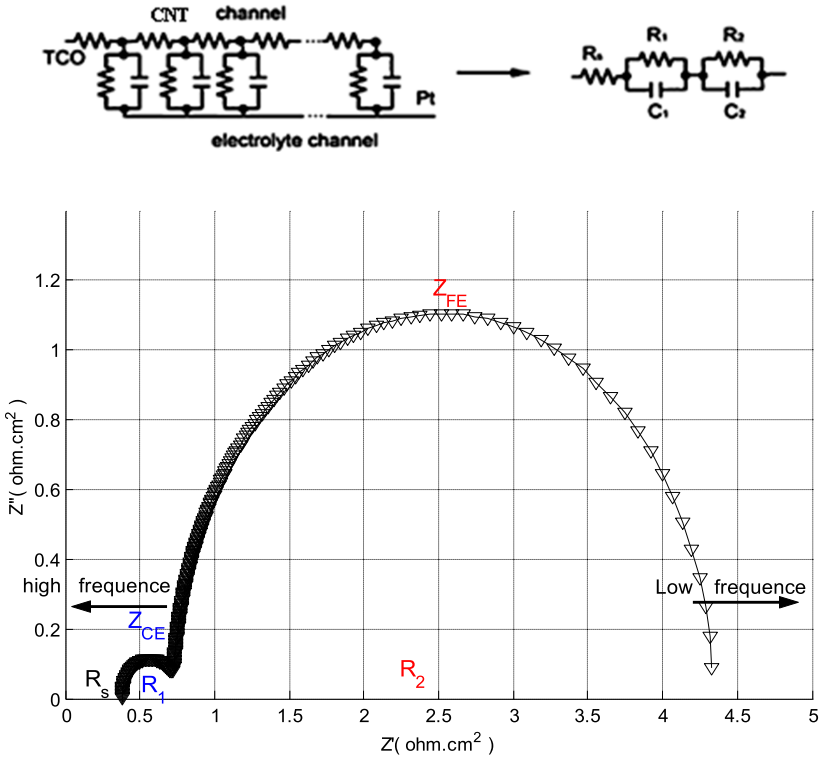

Figure 6. Simulated impedance spectra of CNT-DSC.

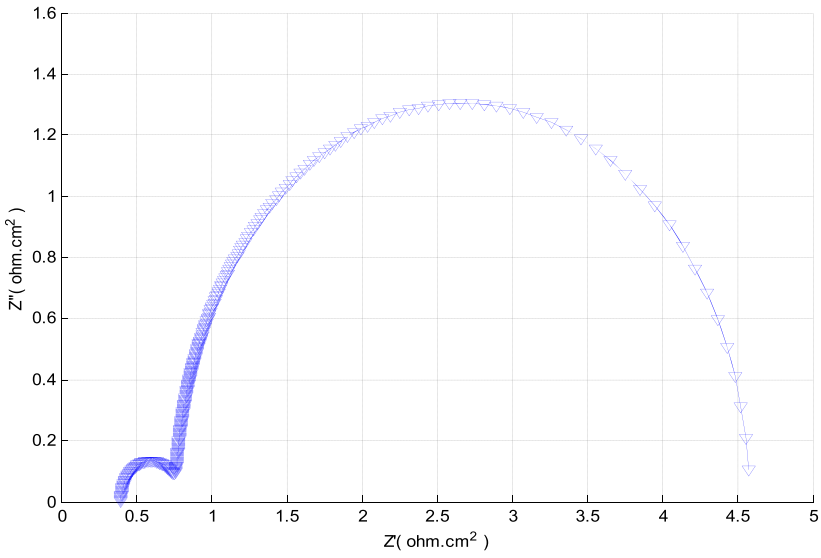

Figure 7. Simulated impedance spectra of TiO_2-DSSC.

Short-circuit current density (J_{sc}) is given as:

$$J_{SC} = \frac{q\varphi L\alpha(\lambda)\left[-L\alpha(\lambda)\cosh\left(\frac{d}{L}\right) + \sinh\left(\frac{d}{L}\right) + L\alpha(\lambda)\exp(-dx)\right]}{(1 - L^2\alpha(\lambda)^2)\cosh\left(\frac{d}{L}\right)} \quad (32)$$

Where q is the charge of the electron, L is electron diffusion length equivalent to $\sqrt{D_e\tau}$, and d is thickness of the thin film [31].

For the working electrode electron density, in case an appropriate functionality is taken into account, cells with external resistive loads can be modelled. Under applied bias, or illumination high intensity, the density of

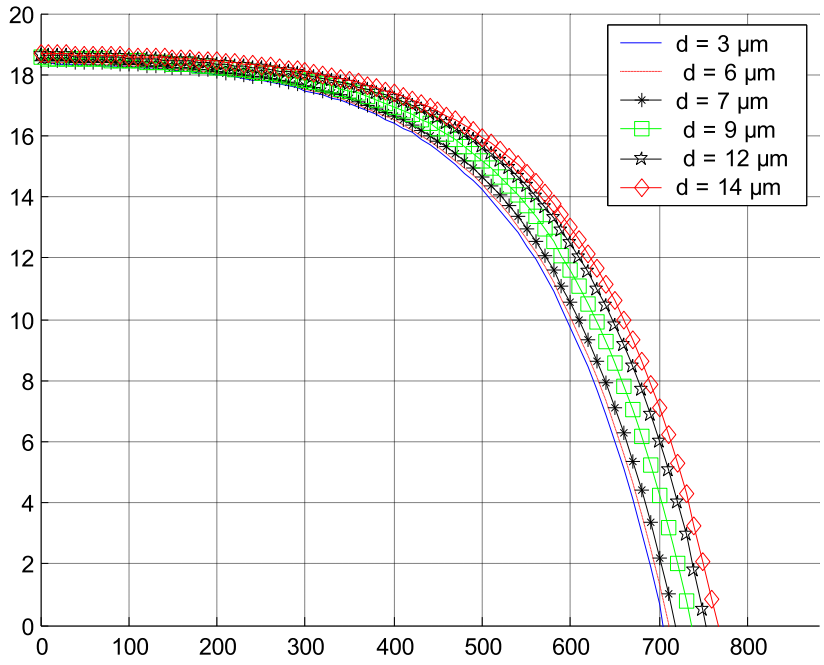

Figure 8. Calculated photo *J–V* characteristics for CNT-DSSC having different electrode thicknesses.

film electrons should increase. Here, the density of electrons as a function of voltage at $x = 0$, $n_e(V)$ is calculated by:

$$n_e(V) = n_0 \exp\left(\frac{q\overline{\alpha}V}{k_B T}\right) \tag{33}$$

Where $\overline{\alpha}$ is a parameter that describes average depth of the trap state energy distribution beneath conduction band (CB).

For a given current density, the value for cell voltage (V) is calculated by equation (35), where $E_R(d)$ is the redox potential at the CE.

$$V = \frac{1}{q}[E_F^n(0) - E_R(l)] \tag{34}$$

The Fermi level, $E_n^F(0)$, for CNT at the TCO/CNT interface (x = 0), is affected by concentration of electron at the interface, $n_e(0)$, equation (35).

$$E_F^n(0) = E_{BC} + k_B T ln\frac{n_e(0)}{N_{BC}} \tag{35}$$

Where N_{CB} is the CNT effective density of states in the CNT conduction band as described in equation (36), knowing m_e is effective mass of electron and h is the Planck's constant [31].

$$N_{BC} = 2\left(\frac{2\pi m_e^* k_B T}{h^2}\right)^{3/2} \tag{36}$$

The model originally used in thin film solar cell simulations [1], allows the steady-state simulation for *J–V* plots, concentration of electro-active species (depth dependent) and current densities for a given DSSC. The numerical solution for the continuity equation (1), combined with equations (32) and (33), together with boundary conditions, yields *J–V* simulated plots [31]. Attention is paid here to see effect of working electrode layer thickness for the CNT-DSSC.

The calculated photo *J–V* plots for CNT-DSSCs, with different CNT working electrode layer thicknesses, are obtained, as shown in figure 8.

The series resistance, R_S, can also be considered into the calculation. In this case, the voltage V used is replaced by $V = V + JAR_S$, where J is photo current density and A the electrode geometrical surface area [31]. Figure 8 describes effect of CNT electrode layer thickness on J-V characteristics, The effect of series resistance has already been reported earlier [31] and is not included here. The results are summarized in table 2. For bench mark purposes, earlier reference values for TiO_2-DSSC system are included for two different thicknesses 7 and 14 μm.

Table 2. Simulated PEC performance parameters (J_{SC}, V_{OC}, *FF* and η) for CNT-DSSCs with different working CNT electrode layer thicknesses, with platinum counter electrode.

Entry number	d_{CNTs} (μm)	J_{SC} (mA cm^{-2}) CNT-DSSC	V_{OC} (mV) CNT-DSSC	FF (%) CNT-DSSC	η (%) CNT-DSSC
1	3	18.38	705	48.70	5.85
2	6	18.39	708	51.15	6.17
3	7	18.4	710	51.81	6.72
4	9	18.53	730	51.85	6.95
5	12	18.58	745	52.10	7.11
6	14	18.63	755	52.47	7.38
7	7[a]	8.22	696	53	3.01
8	14[a]	8.21	689	52	2.95

[a] Using TiO_2 as working electrode layer as reported earlier [36].

Table 2 shows that the PEC characteristics are affected by working electrode thickness in both CNT-DSSC (entries # 1–6) and TiO_2-DSSC (entries # 7–8) systems. Entries 1–6 show that the CNT-DSSC cell exhibits enhancement in PEC characteristics with increased CNT film thickness. Similarly, the literature TiO_2-DSSC cell shows enhancement in PEC characteristics by increasing the working electrode thickness from 7 to 14 μm. Entries 7 and 8) show that the TiO_2-DSSC cell exhibits generally lower PEC characteristics than the TiO_2-DSSC counterpart. As per the CNT-DSSC cell, the increase in PEC characteristics is not too small with film thickness. This means that two opposing factors are affecting performance with thickness increase. The internal resistance across the CNT increases, with film thickness increase, and lowers the J_{SC}, as described earlier [30]. On the other hand, light absorption increases with thickness, which causes higher J_{SC} values. As a balance off, the increase in PEC performance with film thickness is only small. In case of the TiO_2-DSSC, the internal resistance is the dominant factor.

It is thus strongly recommended to devote more theoretical and experimental study on CNT-DSSC systems. Work is underway here to study effects of other parameters, such as type of redox couple, temperature, stability, and others, on the cell performance. Studying capacitance versus voltage (CV) analysis, to improve cell performance, is another area is also underway under way here. Using double and multi- walled CNTs is another issue to study which may add further enhancement to the cell performance. Effect of CNT diameter, edge type, and doping on cell performance is worth to study.

5. Conclusion

A mathematical model for a CNT-DSSC is presented, focusing on effect of CNT working electrode thickness on PEC characteristics. Interfacial charge transport and mass transfer reactions are considered in the study. The theoretical study of the interfacial reaction kinetics helps to describe a system in the form of Faradaic impedance equations. The equations are derived by an electrochemical reaction at the photo-electrode and the counter electrode. The solution to this problem by non-linear programming techniques, such as the Newton-Raphson algorithm, using the numerical calculation is possible. The simulated photo-electrochemical characteristics for the CNT-DSSC are superior to TiO_2-DSSC counterpart.

Acknowledgments

The authors wish to thank Université Amar Telidji de Laghouat. Algérie for financial support. Thanks are due to Dr Ahed Zyoud (of An-Najah N University) with technical editing assistance.

ORCID iDs

Ali Cheknane https://orcid.org/0000-0002-4949-7412
Hikmat S Hilal https://orcid.org/0000-0002-0923-8432

References

[1] Grätzel M 2005 Solar energy conversion by dye-sensitized photovoltaic cells *Inorg. Chem.* **44** 6841–51
[2] Gao F, Wang Y, Shi D, Zhang J, Wang M, Jing X, Humphry-Baker R, Wang P, Zakeeruddin S M and Grätzel M 2008 Enhance the optical absorptivity of nanocrystalline TiO_2 film with high molar extinction coefficient ruthenium sensitizers for high performance dye-sensitized solar cells *J. Am. Chem. Soc.* **130** 10720–8
[3] O'regan B and Grätzel M 1991 A low-cost, high-efficiency solar cell based on dye-sensitized colloidal TiO_2 films *Nature* **353** 737–40
[4] Stathatos E 2013 Progress and perspectives in visible-light-driven photocatalysis *Int. J. Photoenergy* **2013** Article ID 314187
[5] Villanueva J, Anta J A, Guillén E and Oskam G 2009 Numerical simulation of the current−voltage curve in dye-sensitized solar cells *The Journal of Physical Chemistry* C **113** 19722–31
[6] Peter L 2007 Characterization and modeling of dye-sensitized solar cells *The Journal of Physical Chemistry* C **111** 6601–12
[7] Peter L and Wijayantha K 2000 Electron transport and back reaction in dye sensitised nanocrystalline photovoltaic cells *Electrochim. Acta* **45** 4543–51
[8] Dunn H K and Peter L M 2009 How efficient is electron collection in dye-sensitized solar cells? comparison of different dynamic methods for the determination of the electron diffusion length *The Journal of Physical Chemistry* C **113** 4726–31
[9] Soedergren S, Hagfeldt A, Olsson J and Lindquist S-E 1994 Theoretical models for the action spectrum and the current-voltage characteristics of microporous semiconductor films in photoelectrochemical cells *The Journal of Physical Chemistry* **98** 5552–6
[10] Van de Lagemaat J and Frank A 2001 Nonthermalized electron transport in dye-sensitized nanocrystalline TiO_2 films: transient photocurrent and random-walk modeling studies *The Journal of Physical Chemistry* B **105** 11194–205
[11] Nelson J 1999 Continuous-time random-walk model of electron transport in nanocrystalline TiO_2 electrodes *Phys. Rev.* B **59** 15374
[12] Yao J 2015 *Three–Dimensional Zinc Oxide Nanostructure Synthesis* PhD ThesisThe Pennsylvania State University
[13] Zhu H, Wei J, Wang K and Wu D 2009 Applications of carbon materials in photovoltaic solar cells *Sol. Energy Mater. Sol. Cells* **93** 1461–70
[14] Loiseau A, Launois P, Petit P, Roche S and Salvetat J-P 2006 Understanding carbon nanotubes *Lect. Notes Phys.* **677** 495–543
[15] Charlier J-C, Blase X and Roche S 2007 Electronic and transport properties of nanotubes *Rev. Mod. Phys.* **79** 677
[16] Kim J B, Premkumar T, Giani O, Robin J J, Schue F and Geckeler K E 2007 A mechanochemical approach to nanocomposites using single-wall carbon nanotubes and poly (L-lysine) *Macromolecular Rapid Communications* **28** 767–71
[17] McEuen P L, Fuhrer M S and Park H 2002 Single-walled carbon nanotube electronics *IEEE Transactions on Nanotechnology* **99** 78–85
[18] Mawhinney D B, Naumenko V, Kuznetsova A, Yates J T, Liu J and Smalley R 2000 Surface defect site density on single walled carbon nanotubes by titration *Chem. Phys. Lett.* **324** 213–6
[19] Wang S, Zhang Q, Wang R, Yoon S, Ahn J, Yang D, Tian J, Li J and Zhou Q 2003 Multi-walled carbon nanotubes for the immobilization of enzyme in glucose biosensors *Electrochemistry Communications* **5** 800–3
[20] Saito R, Dresselhaus G and Dresselhaus M S 1998 *Physical Properties of Carbon Nanotubes* (London: Imperial College Press)
[21] Baughman R H, Zakhidov A A and De Heer W A 2002 Carbon nanotubes-the route toward applications *Science* **297** 787–92
[22] Che G, Lakshmi B B, Fisher E R and Martin C R 1998 Carbon nanotubule membranes for electrochemical energy storage and production *Nature* **393** 346
[23] Yoshio M, Wang H, Fukuda K, Hara Y and Adachi Y 2000 Effect of carbon coating on electrochemical performance of treated natural graphite as lithium-ion battery anode material *J. Electrochem. Soc.* **147** 1245–50
[24] Wang C, Waje M, Wang X, Tang J M, Haddon R C and Yan Y 2004 Proton exchange membrane fuel cells with carbon nanotube based electrodes *Nano Lett.* **4** 345–8
[25] Stewart D A and Léonard F 2005 Energy conversion efficiency in nanotube optoelectronics *Nano Lett.* **5** 219–22
[26] Veerasamy V S, Amaratunga G A, Park J S, MacKenzie H S and Milne W I 1995 Properties of n-type tetrahedral amorphous carbon (ta-C)/p-type crystalline silicon heterojunction diodes *IEEE Trans. Electron Devices* **42** 577–85
[27] Wu M and Ma T 2012 Platinum-free catalysts as counter electrodes in dye-sensitized solar cells *Chem. Sus. Chem.* **5** 1343–57
[28] Penny M, Farrell T and Please C 2008 A mathematical model for interfacial charge transfer at the semiconductor–dye–electrolyte interface of a dye-sensitised solar cell *Sol. Energy Mater. Sol. Cells* **92** 11–23
[29] Haque S A, Tachibana Y, Klug D R and Durrant J R 1998 Charge recombination kinetics in dye-sensitized nanocrystalline titanium dioxide films under externally applied bias *The Journal of Physical Chemistry* B **102** 1745–9
[30] Anta J A, Casanueva F and Oskam G 2006 A numerical model for charge transport and recombination in dye-sensitized solar cells *The Journal of Physical Chemistry* B **110** 5372–8
[31] Gacemi Y, Cheknane A and Hilal H S 2013 Simulation and modelling of charge transport in dye-sensitized solar cells based on carbon nano-tube electrodes *Phys. Scr.* **87** 035703
[32] Zhang D, Ryu K, Liu X, Polikarpov E, Ly J, Tompson M E and Zhou C 2006 Transparent, conductive, and flexible carbon nanotube films and their application in organic light-emitting diodes *Nano Lett.* **6** 1880–6
[33] Pan B and Xing B 2008 Adsorption mechanisms of organic chemicals on carbon nanotubes *Environmental Science & Technology* **42** 9005–13
[34] Villanueva-Cab J, Oskam G and Anta J 2010 A simple numerical model for the charge transport and recombination properties of dye-sensitized solar cells: a comparison of transport-limited and transfer-limited recombination *Sol. Energy Mater. Sol. Cells* **94** 45–50
[35] Andrade L, Sousa J, Ribeiro H A and Mendes A 2011 Phenomenological modeling of dye-sensitized solar cells under transient conditions *Sol. Energy* **85** 781–93
[36] Topič M, Čampa A, Filipič M, Berginc M, Krašovec U O and Smole F 2010 Optical and electrical modelling and characterization of dye-sensitized solar cells *Current Applied Physics* **10** S425–30
[37] Filipič M, Berginc M, Smole F and Topič M 2012 Analysis of electron recombination in dye-sensitized solar cell *Current Applied Physics* **12** 238–46
[38] Thavasi V, Renugopalakrishnan V, Jose R and Ramakrishna S 2009 Controlled electron injection and transport at materials interfaces in dye sensitized solar cells *Materials Science and Engineering: R: Reports* **63** 81–99
[39] Wei-Qing L, Zhong-Guan L, Dong-Xing K, Lin-Hua H and Song-Yuan D 2013 Wide frequency range diagnostic impedance behavior of the multiple interfaces charge transport and transfer processes in dye-sensitized solar cells *Electrochim. Acta* **88** 395–403
[40] Itagaki M, Nakano Y, Shitanda I and Watanabe K 2011 Faradaic impedance to analyze charge recombination in photoelectrode of dye-sensitized solar cell *Electrochim. Acta* **56** 7975–83
[41] Itagaki M, Hoshino K, Nakano Y, Shitanda I and Watanabe K 2010 Faradaic impedance of dye-sensitized solar cells *J. Power Sources* **195** 6905–23

[42] Bastida J R 1984 *Field Extensions and Galois Theory, volume 22 of Encyclopedia of Mathematics and its Applications* (Massachusetts: Addison-Wesley, Reading)
[43] Weber H J and Arfken G B 2003 *Essential Mathematical Methods for Physicists* (NY: ISE, Academic Press)
[44] Seeger K 2013 *Semiconductor Physics* (NY: Springer Science & Business Media)
[45] Peter L M 2007 Dye-sensitized nanocrystalline solar cells *Physical Chemistry Chemical Physics* **9** 2630–42
[46] Hagfeldt A and Graetzel M 1995 Light-induced redox reactions in nanocrystalline systems *Chemical Reviews* **95** 49–68
[47] Rodríguez M E G 2011 *Photoelectrochemical characterization of dye solar cells based on nanostructured ZnO substrates* PhD ThesisUniversidad Pablo de Olavide, Spain
[48] Hauch A and Georg A 2001 Diffusion in the electrolyte and charge-transfer reaction at the platinum electrode in dye-sensitized solar cells *Electrochim. Acta* **46** 3457–66
[49] Bay L, West K, Winther-Jensen B and Jacobsen T 2006 Electrochemical reaction rates in a dye-sensitised solar cell—the iodide/tri-iodide redox system *SolarEnergy Materials and Solar Cells* **90** 341–51
[50] Macagno V, Giordano M and Arvia A 1969 Kinetics and mechanisms of electrochemical reactions on platinum with solutions of iodine-sodium iodide in acetonitrile *Electrochim. Acta* **14** 335–57
[51] Boschloo G and Fitzmaurice D 1999 Spectroelectrochemical investigation of surface states in nanostructured TiO_2 electrodes *The Journal of Physical Chemistry* B **103** 2228–31